

Morphology control of nickel oxalate by soft chemistry and conversion to nickel oxide for application in photocatalysis†

Cite this: DOI: 10.1039/c3ra21978j

Soumyadipta Rakshit,^a Sayantani Chall,^a Soumya Sundar Mati,^a Anirban Roychowdhury,^b S.P. Moulik^a and Subhash Chandra Bhattacharya^{*a}

The present work provides an effective methodology for controlled room-temperature aqueous synthesis of nickel oxalate (NiOX) nanosheets and nanoflakes in the presence of anion rich self-assembled bilayers of catanionic surfactant comprising of anionic sodium dodecyl sulfate (SDS) and cationic cetyltrimethylammonium bromide (CTAB). Encouragingly alteration of the CTAB/SDS ratio played an extraordinary role to form nanoflakes and nanosheets of NiOX. Our synthetic approach is combined with calcination to produce antiferromagnetic spherical and hexagonal nickel oxide (NiO) nanoparticles (NPs) as the end product. Synthesized nanostructured NiOX and NiO were characterized by X-ray diffraction study (XRD), energy dispersive X-ray spectroscopy (EDS), field emission scanning electron microscopy (FESEM) and transmission electron microscopy (TEM). TEM studies illustrated that spherical NiO NPs have an average size around 5–10 nm and that of hexagonal NiO NPs have average width of about 22–27 nm. Temperature and field dependent magnetic properties of spherical and hexagonal NiO nanomaterials (NMs) were measured by using a SQUID magnetometer which revealed canted antiferromagnetic and spin glass nature, respectively. In addition, we report photocatalytic activity of NiO NMs, investigated on the photodegradation of phenol under ambient conditions, and as expected, the NiO having largest surface area showed best catalytic efficiency. This biomimetic catanionic surfactant inspired approach which require only metal ions as reactants have a definite potential towards an alternative, simple way of synthesizing metal oxide NMs.

Received 29th August 2012,
Accepted 5th February 2013

DOI: 10.1039/c3ra21978j

www.rsc.org/advances

1. Introduction

Morphology-controlled synthesis of inorganic one-dimensional (1D) and two-dimensional (2D) nanoscale building blocks with controlled size and shape into 2D complex structures is of extensive research interest. It is expected that if the morphology and assembly mode of the original building units can be controlled, then those of their secondary architecture would be adjustable. Electronic, optical, magnetic and catalytic properties of a functional material are highly responsive on tuning the morphology (including dimensionality and shape) of nanostructured materials.^{1–5} Therefore, research on cost effective morphology-controlled and assembly-designed synthesis needs to be emphasized for enabling

novel intrinsic properties and applications of nanomaterials (NMs).

Transition metal oxides are key materials in catalysis, microelectronic, optical and magnetic applications.^{6–9} In our work we have focused on nickel oxide since it is one of the relatively few metal oxides with p-type semiconductivity and having a stable wide band gap. It has extensive applications as a catalyst,¹⁰ as electrode material for lithium ion batteries and fuel cells,^{11–13} in electrochromic films,¹⁴ electrochemical supercapacitors,^{15,16} magnetic materials,¹⁷ gas sensors¹⁸ and biosensors.¹⁹

Morphology controlled transformation of precursors has proven to be a promising approach for the synthesis of NiO nanostructures. Recent reports on solid-state calcination of well designed precursors into nanoporous NiO clearly exemplify a very close relationship between precursors and products and further inspire the concept of precursor controlled synthesis of well defined NiO nanostructures. Nickel hydroxides (Ni(OH)₂) and oxalates (NiOX) are the mostly used precursors for synthesising NiO nanoparticles (NPs) after thermal conversion. Gao *et al.* reported synthesis of α -Ni(OH)₂ and NiO with different morphologies through a ethylene glycol mediated self-assembly approach,²⁰ synthesis

^aDepartment of Chemistry, Jadavpur University, Kolkata 700032, India.

E-mail: sbjuchem@yahoo.com; schhattacharyya@chemistry.jdvu.ac.in; Fax: 91(033) 24146584; Tel: 033 2414 6223

^bUGC - DAE Consortium for Scientific Research, Kolkata Centre, 111/LB-8, Bidhanagar, Kolkata 700098, India

† Electronic supplementary information (ESI) available: Figures showing energy dispersive X-ray spectra of NiOX I and NiO I, FESEM images of nickel oxides, plot of χT vs. T for NiO I, photoluminescence of residual phenol in presence of NiO I over three cycles, FESEM image and XRD pattern of commercial NiO have been included. See DOI: 10.1039/c3ra21978j

of NiO nanobelts, nanowires, nanoplates and hollow spheres were also reported by various other groups.^{21,22} Vaidya *et al.* reported solvent effects in reverse micelle templated shape controllable synthesis of nano-spheres, -cubes and -rods of nickel oxalate to prepare NiO NPs.²³ However, insurmountable limitations of most of the synthesis methods (excluding thermal decomposition) in terms of large scale production, complicated synthesis steps and comparatively high cost, triggered us to opt for an alternative facile and promising route. Moreover this approach is suitable for mass production for future large-scale application.

Since surface active compounds enable soft chemical and biomimetic approaches,²⁴ self-assembled well defined structures of surfactants has been taken advantage of for designing and synthesis of inorganic nanodimensional materials. They are used as a kind of template for the synthesis and have the ability for compartmentalization of the synthesised nanostructures, which alters the product states and reduces the reaction dimensionalities.²⁵ Aqueous mixtures of oppositely charged surfactants exhibit interesting phase behaviour and properties because of the tunability of the oppositely charged head groups. At high surfactant concentrations and above the Krafft boundary of the mixtures, these systems can form several types of microstructures, namely lamellar and cubic phases, vesicles, spheres, rod like structures which are not present in the individual surfactant–water binary system.^{26,27} At low concentrations (generally below 5.0 wt%) the behaviour of these catanionic systems is dominated by phase separation, with the formation of a highly insoluble precipitate (solid catanionic) at and around equimolarity.²⁸ However, with an excess of one of the surfactants the precipitate dissolves to yield heterogeneous self-assembled aggregates of different structures. In recent years efforts have been made on the synthesis of nanoparticles within unique catanionic reverse micelles.^{29–31} However despite the development of strategies for synthesis of nanosheets, we are reporting for the first time a large-scale room-temperature soft chemical nonhazardous synthesis of nickel oxalate polycrystalline nanosheets.

In the present work, we have synthesized NiOX in dispersed catanionic systems which show a promising potential in morphological and hierarchical synthesis of nanostructured materials. Here, we discuss the role of catanionic surfactant in morphology controlled synthesis. Pure phase synthesis of the desired material was characterised by employing X-ray diffraction (XRD) study, thermogravimetry–differential thermal analysis (TG–DTA), field emission scanning electron microscopy (FESEM) and transmission electron microscopy (TEM) analysis. Furthermore, we have assessed the photocatalytic performance of NiO NPs during the photoinduced oxidation of phenol.

Photocatalysis is an effective method for the treatment of contaminants and pollutants, especially for the removal of organic compounds, since it works in ambient conditions of temperature and pressure without forming any kind of sludge which otherwise create different pollutant problems. Degradation of these toxic substances by photocatalysis in

aqueous medium could be the basis of waste treatment.^{32,33} Semiconductor photocatalysts offer a huge potential for elimination of organic pollutants in water.³⁴ The photocatalytic activity of NiO with high surface area so far has been insignificant.³⁵ BET surface areas of NiOs were also measured to correlate their photocatalytic activity with surface area.

2. Experimental

2.1. Chemicals

The precursor metal salts, nickel(II) nitrate hexahydrate ($\text{Ni}(\text{NO}_3)_2 \cdot 6\text{H}_2\text{O}$, 99.9%) and sodium oxalate ($\text{Na}_2\text{C}_2\text{O}_4$, 98%) were purchased from E. Merck. The two surfactants, cetyltrimethylammonium bromide (CTAB, 99.9%) and sodium dodecyl sulfate (SDS, 99.9%) were purchased from Aldrich and BDH, respectively, and were used as received. Chloroform and acetone of analytical grade used in this work were purchased from E. Merck and dried by standard procedures.³⁶ Commercial NiO nanopowder (98%, spherical) was purchased from SRL, India. The water used was treated with a Millipore-Q water purification system.

2.2. Synthesis of nickel oxalate and nickel oxide nanomaterials

In the present work, nanostructured NiO was synthesized in two steps. In the first step, nanocrystalline precursor NiOX was prepared using two different synthetic strategies namely *dispersion* method (method I) and *in situ* method (method II) and in the next step, oxalates (NiOX I obtained from method I and NiOX II from method II) were subjected to thermal decomposition. In the first synthetic approach, growth of nickel oxalate was realised through templated dispersed catanionic surfactant; however, in the second approach, the mode of synthesis of the catanionic was different. In both the methods we used three different SDS/CTAB volume ratios (60/40, 65/35, 70/30) to investigate the role of catanionic surfactant during the synthetic procedure.

In method I, SDS (0.05 mol dm^{-3}) and CTAB (0.05 mol dm^{-3}) were added in a volume ratio 65/35 in water to prepare a dispersed catanionic solution (*dispersion* method). The final concentration of SDS and CTAB in the solution were 0.8125 and 0.4375 mM which were lower than their respective critical micellar concentrations (CMC).^{37,38} To this solution $\text{Ni}(\text{NO}_3)_2$ (0.05 mol dm^{-3}) and $\text{Na}_2\text{C}_2\text{O}_4$ (0.05 mol dm^{-3}) were added and stirred for 6 h. The product *i.e.*, nickel oxalate was separated by centrifugation, washed first with chloroform and then with acetone to make it surfactant free. The washed material was dried at 40°C in an oven.

In method II, a substantially modified approach of the previous strategy was employed where the template and product were generated *in situ* (*in situ* method). During the synthesis, two individual solutions were prepared. Solution A containing CTAB (0.05 mol dm^{-3}), Ni^{2+} (0.05 mol dm^{-3}) and solution B comprising of SDS (0.05 mol dm^{-3}), $\text{C}_2\text{O}_4^{2-}$ (0.05 mol dm^{-3}) in water were mixed together at the previous surfactant concentrations and continuously stirred for 6 h. Similar SDS/CTAB ratios were also investigated. The product was centrifuged followed by washing and drying as before. In

both routes the concentration of NiC_2O_4 was 4.0 mmol dm^{-3} . The prepared green powders were calcined at 450°C for 3 h to obtain black NiO powders. The optimal annealing temperature was determined by thermogravimetric measurements to ensure complete conversion of precursor oxalates to oxide.

2.3. Instrumentation

The surface morphology of NiO nanoparticles was examined by high-resolution transmission electron microscopy (HRTEM, Model: JEOL-JEM-2100) at an accelerating voltage of 200 kV and by field emission scanning electron microscopy (Hitachi S-4800, Japan). The structural studies of the precursor oxalates as well as the calcined oxide products were performed with an X-ray diffractometer using $\text{Cu-K}\alpha$ radiation ($\lambda = 0.15406 \text{ nm}$). Thermogravimetry–differential thermal analysis was carried out in a Perkin Elmer Pyris Dymond TGA/DTA system in air with a heating rate of $10^\circ\text{C min}^{-1}$. BET (Brunauer–Emmett–Teller) surface area measurements were performed with an Autosorb iQ (Quantachrome Inc., USA) gas sorption system at 77 K. Magnetic properties of nickel oxide were measured by a SQUID magnetometer [MPMS XL7, Quantum Design, USA]. Absorption spectra of as synthesised NiO were recorded with a Shimadzu UV-1601 PC UV-Vis spectrophotometer using matched quartz cells. The photoluminescence spectral analysis of the residual phenol was performed using a Fluorolog FIIA spectrofluorimeter (Spex Inc, NJ, USA) with a slit width of 2.5 mm.

2.4. Photocatalytic measurement

The photocatalytic activity of as-synthesized NiO nanoparticles (NPs) was measured by decomposing phenol at room temperature. A tubular beaker (capacity 50 mL) was used as the photoreactor. The reaction system contained 22.0 mg of NiO nanoparticles and 30 mL of a dilute aqueous phenol solution (0.02 mg L^{-1}), which was initially stirred in the dark for 1 h to reach the adsorption equilibrium of phenol. The reaction system was then exposed to a source of UV radiation and the degradation of the photoluminescent peak of phenol at $\sim 305 \text{ nm}$ was monitored with time.

After the first use of the NiO, it was filtered and then washed with water along with ultrasonication several times and it was then centrifuged. The centrifuged NiO was then dried at 120°C for 5 h in an electric oven. Recovered NiO having same size and shape was then reused for new degradation batch having

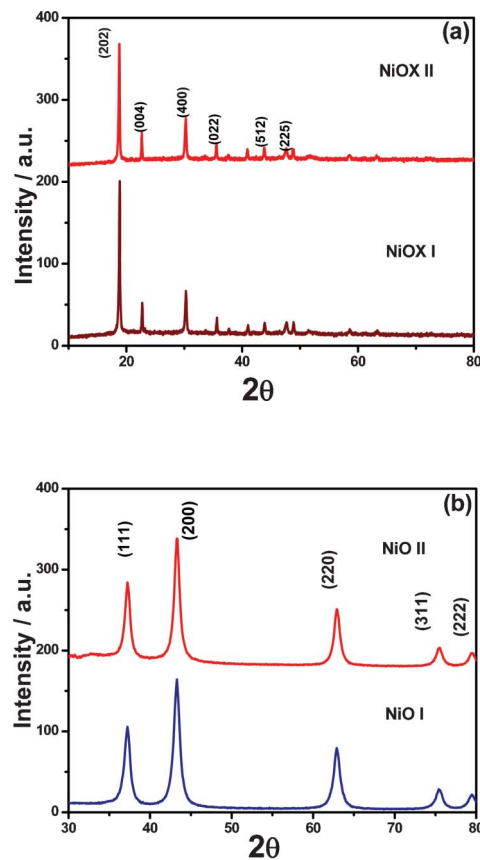


Fig. 1 X-Ray diffraction pattern of (a) as-synthesized NiOX I, NiOX II and (b) NiO I, NiO II.

the same phenol concentration (0.02 mg L^{-1}) and degradation of phenol was monitored by photoluminescence.

3. Results and discussion

3.1. Characterization of NiOX and NiO

The overall crystallinity and phase composition of the as synthesized nanostructured NiOX and NiO were initially analysed by X-ray powder diffraction (XRD) (Table 1).

Table 1 Values of d -spacings (\AA) obtained from XRD patterns and HRTEM analysis of nickel oxalate and nickel oxide prepared by methods I and II

Sample	Space group	hkl	Obs. d_{hkl} (XRD)/ \AA	Obs. d_{hkl} (TEM)/ \AA	Standard $d_{hkl}^a/\text{\AA}$
NiOX I	<i>Cccm</i>	202	4.711	—	4.770
		004	3.906	—	3.940
		400	2.953	—	2.959
NiOX II	<i>Cccm</i>	202	4.727	—	4.770
		004	3.918	—	3.940
		400	2.953	—	2.959
NiO I	<i>Fm\bar{3}m</i>	111	2.413	2.41	2.410
		200	2.087	2.08	2.088
NiO II	<i>Fm\bar{3}m</i>	111	2.413	2.42	2.410
		200	2.086	2.08	2.088

^a JCPDS 14-0742 and 47-1049.

According to the JCPDS card (14-0742), all the diffraction peaks as displayed in Fig. 1a, could readily be indexed to a pure phase NiOX having orthorhombic lattice structure (lattice parameters: $a = 11.84 \text{ \AA}$, $b = 5.345 \text{ \AA}$, $c = 15.716 \text{ \AA}$, $Z = 8$, space group Ccm). For NiOX I and II the diffraction peak of (202) was the strongest of the diffraction peaks shown in the XRD pattern (Fig. 1a), which indicated a preferential growth. In the earlier works of Wang *et al.*²¹ and Vaidya *et al.*,²³ they reported a monoclinic phase of nickel oxalate dihydrate prepared by solvothermal and reverse micellar routes, respectively, having lattice parameters $a = 11.77 \text{ \AA}$, $b = 5.333 \text{ \AA}$, $c = 9.833 \text{ \AA}$, $\beta = 127.2^\circ$, $Z = 4$, space group $C2/c$ which were contrary with our present findings. In Fig. 1b, the three major diffraction peaks could perfectly be indexed as (111), (200) and (220) crystal planes of the cubic structure of highly crystalline NiO which was in good agreement with the literature value (JCPDS 47-1049) and no obvious diffraction peaks assignable to other impurities could be detected. The average grain sizes of NiO I and NiO II, calculated from X-ray line broadening (using the Debye–Scherrer equation²³) on the basis of the strongest (200) reflection are 11 and 20 nm, respectively.

Corresponding EDX spectra further confirmed the elemental composition of the precursor NiOX (Fig. S1a, ESI†) and the final product, NiO (Fig. S1b, ESI†). Fig. S1b† highlighted the presence of only nickel and oxygen peaks, with no other relevant elements were present which clearly demonstrated that the proposed method was a clean, simple and effective chemical process. Analysis of the EDX of NiOX I (Fig. S1a, ESI†) and NiO I (Fig. S1b, ESI†) prepared in 65/35 SDS/CTAB ratio

indicated an atomic ratio of 86% Ni and 14% O in NiOX and 76.7% Ni and 23.3% O in NiO.

3.2. Thermogravimetric (TG–DTA) investigation

To elucidate the exact chemical structure of nickel oxide precursors, we studied the thermal behaviour of NiOX I and NiOX II. The thermogravimetry–differential thermal analysis (TG–DTA) curves of the as-prepared precursors are shown in Fig. 2a and b. Both the curves of the sheet-like oxalate precursors showed two step weight losses. For NiOX I, the initial weight loss of about 19.8% at 165–220 °C associated with an endothermic peak at 214.2 °C represented the removal of the two crystal water molecules. Likewise, for NiOX II, in the first step, 18.3% weight loss occurred at 165–225 °C with an endothermic maximum at 216.6 °C. For both the precursors, a second step weight loss at around 325 °C (40.76 and 36.7%, respectively) corresponded to the elimination of CO₂.³⁹ Release of CO₂ molecules from the oxalates at high temperature region was exothermic in nature and gave rise to peaks at 346.1 and 356.1 °C, respectively. This slight difference in peaks could be assigned to their difference in sizes.

3.3. Electron microscopy analysis: FESEM and TEM

After ascertaining the synthesis of chemically pure phase NiOX and NiO NMs we further attempted to visualize the variation of morphologies and to conclusively determine the structural patterns of the precursors and final products, FESEM and TEM measurements were carried out. Morphology evolution of nickel oxalate samples prepared at an SDS/CTAB ratio of 60/40 showed nanoflakes with an average size of $230 \pm 20 \text{ nm}$ for method I and of $190 \pm 20 \text{ nm}$ for method II (Fig. 3a and 4a). Fig. 3b and 4b show representative FESEM images of the single nanosheet structures (SDS/CTAB = 65/35) of NiOX I and II having average size of 210 ± 20 and $490 \pm 40 \text{ nm}$. At an SDS/CTAB ratio of 70/30, nickel oxalate formed multilayered nanosheets with average size of $260 \pm 20 \text{ nm}$ for NiOX I (Fig. 3e) and $260 \pm 25 \text{ nm}$ for NiOX II (Fig. 4e). We report the sizes of NiOXs with standard deviations (Table 2) after repeating the preparations three times, showing excellent reproducibility of this catanionic system. Clearly the ratios of SDS/CTAB catanionic template undoubtedly control the morphology and size of the precursor oxalate. Furthermore, the geometrical structures of NiO were elucidated by transmission electron microscopy (TEM) which clearly reinforced that no structure variation of NiO was obtained after calcination (Fig. 3d, f and 4d, f) for oxalate nanoflakes and multilayered nanosheets of precursor oxalates. However, for single nanosheets we obtained granular (NiO I) and hexagonal nickel oxide (NiO II) (Fig. 3d and 4d, SDS/CTAB = 65/35).

During subsequent synthesis we preferably chose 65/35 (SDS/CTAB) volume ratio for our synthesis since in this particular ratio the dispersed anionic rich catanionic surfactant gave rise to highest stability along with a two dimensional structure.⁴⁰

On the basis of reaction conditions and parameters we herein propose a plausible formation mechanism of nickel oxalate (Scheme 1). Surfactant concentrations are one of the controlling parameters of the phase behavior of cationic/anionic surfactant mixtures⁴⁰ which in turn organize pattern-

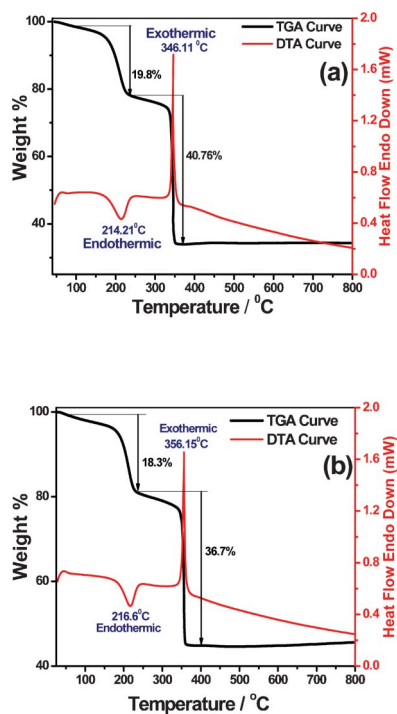


Fig. 2 TG–DTA curves of (a) NiOX-I and (b) NiOX-II nanosheets prepared at a SDS/CTAB ratio of 65/35.

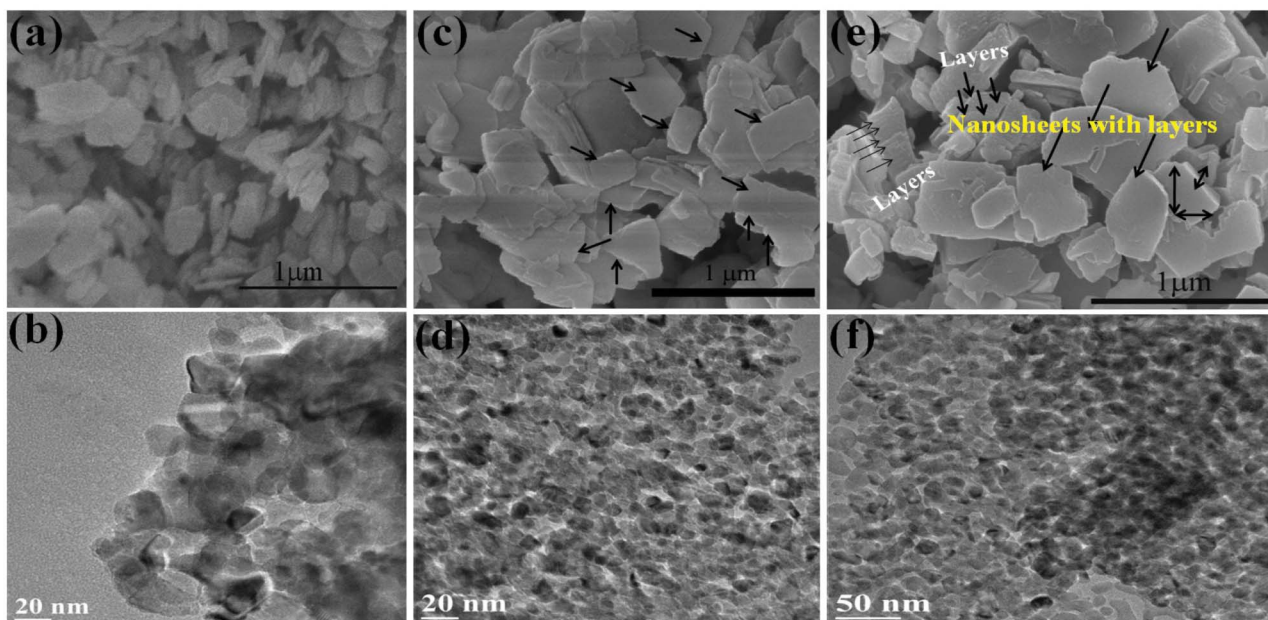


Fig. 3 FESEM images of as-synthesized NiOX I (*dispersion* method) with SDS/CTAB ratios (a) 60/40, (c) 65/35, (e) 70/30; TEM images of corresponding NiOs prepared after calcination of NiOX I, SDS/CTAB ratios (b) 60/40, (d) 65/35, (f) 70/30.

ing of different morphologies of the nanomaterials. As a consequence of dynamic electrostatic interaction, between two oppositely charged head groups (here, CTAB and SDS) catanionic complexes formed in solutions. In combination CTAB and SDS are known to form uni- and multi-lamellar vesicles which with higher proportion of SDS progressively become unstable as the molar composition tends towards 1 : 1

with precipitation.^{40–43} Inorganic ions are known to form plate and sheet like morphologies⁴⁴ in such media. In both the methods I and II (in catanionic template forming media) formation of NiOX is governed by the above route. The mixed lamellar vesicular template supported formation of large nanosheets of NiOX as schematically presented. Penetration of both Ni^{2+} and $\text{C}_2\text{O}_4^{2-}$ in the bilayered head group region of

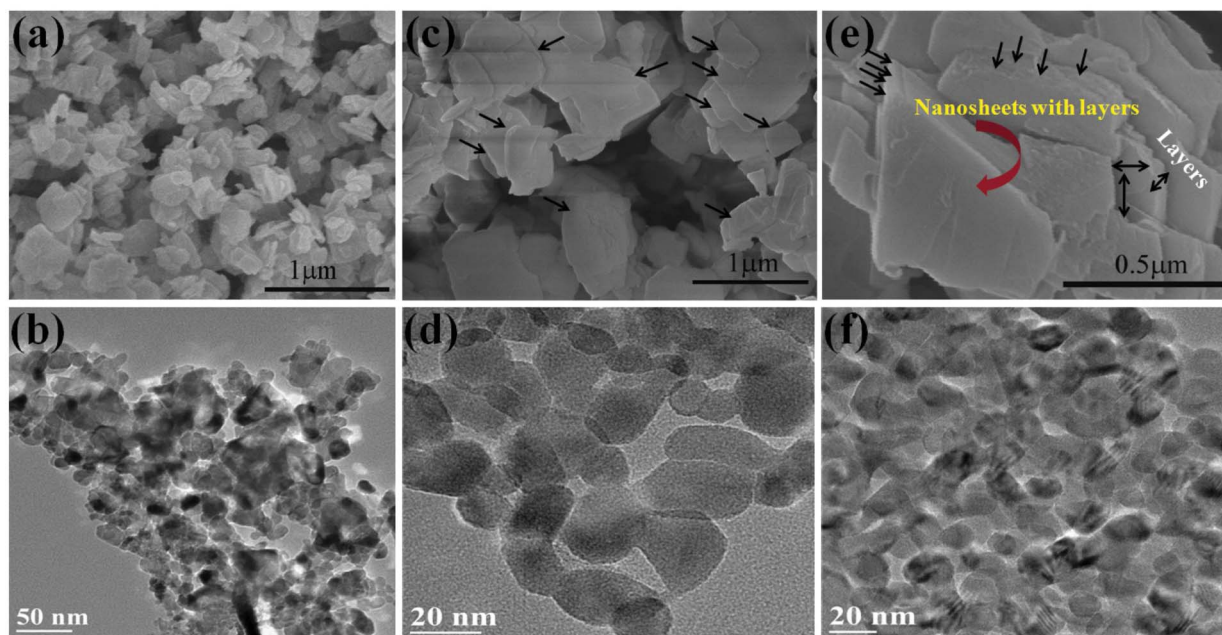


Fig. 4 FESEM images of as-synthesized NiOX II (*in situ* method) with SDS/CTAB ratios (a) 60/40, (c) 65/35, (e) 70/30; TEM images of corresponding NiOs prepared after calcination of NiOX II, SDS/CTAB ratios (b) 60/40, (d) 65/35, (f) 70/30.

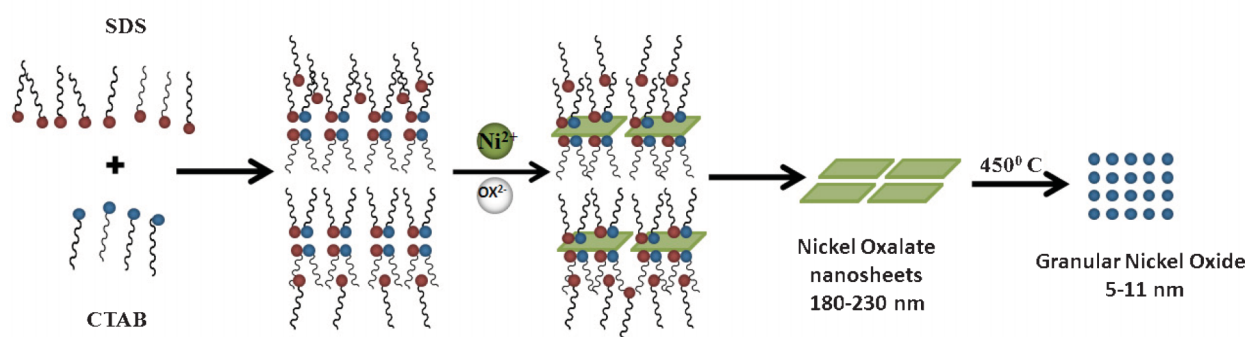
Table 2 Structural variation of nickel oxalate (NiOX) and nickel oxide (NiO) with the variation of volume ratio of SDS/CTAB

Sample	Ratio		Dispersion		In situ	
	SDS	CTAB	Morphology	Size/nm	Morphology	Size/nm
NiOX	60	40	Nanoflakes	200–250	Nanoflakes	170–210
	65	35	Nanosheet	180–230	Nanosheet	450–530
	70	30	Nanosheet with layers	250–280	Nanosheet with layers	240–280
NiO	60	40	Granular	14–16	Granular	15–17
	65	35	Granular	5–10	Hexagonal	22–27
	70	30	Granular	12–14	Granular	12–14

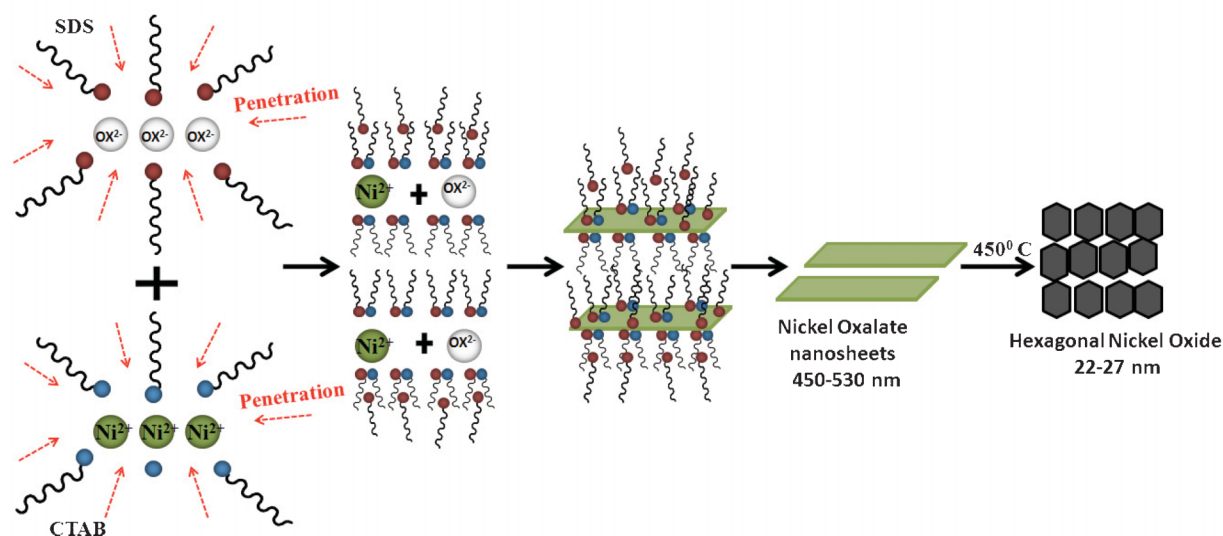
the systems produce NiOX, and depths of the lamellar vesicles determine the sheets' dimensions until destabilization of the overall structure arose for solubility reasons. The volume ratio of SDS and CTAB has a primary influence on the formation and size of the products. In case of a 60/40 ratio the numbers of cationics formed were a maximum, which indicated

denser cationic situation and low concentration of stabilizer SDS, resulting in quicker formation of thinner flaky products. Initially formed larger plate-like structures were amenable to form larger products upon removal of surfactant and calcination under controlled thermal condition.

Method I: Dispersion



Method II: In situ

**Scheme 1** Schematic representation of formation of nickel oxalate by methods I and II in dispersed cationic (SDS/CTAB ratio 65/35).

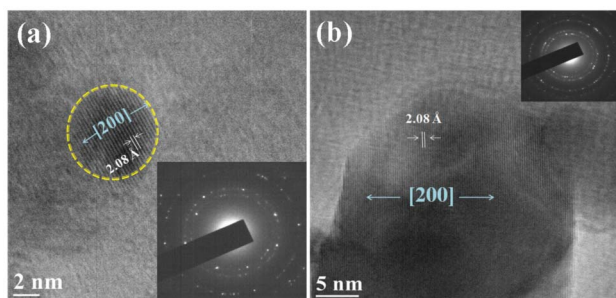


Fig. 5 HRTEM images of granular and hexagonal nickel oxide nanoparticles prepared by method I (a) and method II (b) having interplanar spacing (d_{hkl}) 2.08 Å [200]; inset shows the SAED patterns.

A large difference in size of the precursors can result a difference in grain size and morphology in the synthesis of secondary architectures.⁴⁵ Nickel oxalates with different morphology but comparable size led to granular NiO with a very little difference in grain size but nickel oxalate having size in the range 450–530 nm resulted in hexagonal NiO. As the size difference of NiO nanosheets can produce two distinct morphologies, we can conclude in a generalised way that the size of precursor played the key role towards the morphology of calcined product rather than the morphology of the precursor.

Fig. 5a, b and 6a, b display the most prominent lattice planes present and have been indexed and correspond to 200 and 111 planes obtained from careful HRTEM observation, consistent with our XRD results. This observation coupled with selected area electron diffraction patterns, shown as an inset in Fig. 5a, b and 6c, d give the idea of the overall polycrystallinity of the nickel oxides.

The texture properties were further elucidated by N_2 sorption analysis. The specific surface area of NiO prepared in method I (granular shaped) was much higher than that

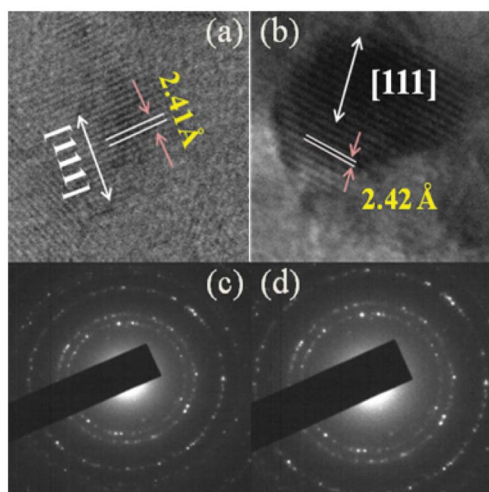


Fig. 6 HRTEM images of NiO prepared by method I (a) and method II (b) having interplanar distances of 2.41 and 2.42 Å [111], respectively, and (c), (d) their corresponding SAED patterns.

prepared in method II (hexagonal shaped) for SDS/CTAB ratio 65/35. The measured surface areas are given in Table 3. The higher surface area for NiO I may be attributed to its smaller grain size (Fig. S2a, ESI†).

3.4. Optical properties

UV-Vis absorption spectroscopy is an important method to reveal the energy structures and optical properties of semiconductor nanocrystals. The absorption spectra of as-synthesized granular and hexagonal NiO prepared at SDS/CTAB ratio 65/35 is illustrated in Fig. 7. The above spectra showed a 9 nm blue shift for NiO I relative to NiO II, which was due to significant difference in crystal size associated with NiO nanoparticles. The strong absorption peaks at 322 nm for NiO I and 331 nm for NiO II gave the absorption energy corresponding to a band gap (E_g) of 3.85 and 3.74 eV, respectively. The increase in the band gap of the NiO nanoparticles compared to bulk material was indicative of a quantum confinement effect of the nanocrystallites.

3.5. Magnetic properties

Magnetic properties of both the nickel oxides were measured by a SQUID magnetometer over a wide range of temperature and magnetic field. We observed a huge change in magnetic properties with the change in morphology and grain size. Temperature-dependent magnetization measurements were carried out from 10 to 300 K at an applied field of 100 Oe for both the samples under zero-field-cooled (ZFC) and field-cooled (FC) conditions.

For NiO I ZFC and FC magnetization (M_{ZFC} and M_{FC}) curves followed the same nature and both showed a sharp increase after 30 K and increased monotonically up to the lowest experimentally possible temperature. A bifurcation between the ZFC and FC curves was observed in NiO II which was not pronounced in the ZFC/FC curves of NiO I. Similar (Fig. 8a) behavior of the ZFC and FC curves were reported earlier for other oxide materials.^{46,47} A plot of χ^{-1} vs. T of NiO I (Fig. 8a inset) presents antiferromagnetic behaviour. The increase in magnetization value at lower temperature suggested the presence of uncompensated antiferromagnetic spin at the nanoscale.⁴⁸ Furthermore a plot of χT vs. T (Fig. S3, ESI†) clearly demonstrated canted antiferromagnetic behaviour.⁴⁹ In order to determine the magnetic property more fully hysteresis loops of the NiO I were measured at 10, 100 and 300 K (Fig. 8c). A clear $M-H$ loop was observed at 10 K which clearly showed a nanoscale ferromagnetic (FM) interaction in consequence of canting in the surface region.

For NiO II ZFC and FC magnetization curves were found to bifurcate at around 206 K (T_{bf}) (Fig. 8b). It is well known that the bifurcation temperature T_{bf} corresponds to the largest particles in the size distribution. At 12 K (T_2) and 56 K (T_1) in the M_{ZFC} curve two distinct maxima were observed (Fig. 8b) for which the first (T_2) was very sharp compared to the other (T_1). The M_{FC} curve showed a steep low temperature rise starting at about 25 K and then increased monotonically till the lowest temperature of measurement. The spin glass like behavior of the M_{ZFC} curve at around 12 K indicated collective freezing of disordered spins in the surface region and that around 58 K was attributed to the presence of a ferromagnetic core

Table 3 Structural and catalytic information of nanostructured NiO.

Sample	d_{XRD}/nm	d_{TEM}/nm	$S_{\text{BET}}/\text{m}^2 \text{g}^{-1}$	k/min^{-1}	% PhOH degraded
NiO I	11	5–10	66	1.72×10^{-2}	82.10
NiO II	20	22–27	28	1.17×10^{-2}	69.22
Commercial NiO	45	32–37 ^a	11	5.82×10^{-3}	44.10

^a Obtained from FESEM (Fig. S5a, ESI†).

consisting of a non-saturating component.⁵⁰ The origin of such a maximum at low temperature (12 K) might be due to the ordering of small magnetic clusters at the particle surface, inducing strong intraparticle interactions, which led to a frustrated magnetic state.⁵¹ Beyond T_1 the thermal energy surpassed the applied field effect leading to superparamagnetic relaxation.⁵² To obtain a more detailed view of this interesting magnetic property the hysteresis loops were measured at different temperatures (10, 100 and 300 K). At 10 K a hysteresis loop with a low value of coercivity was evident but at 300 K it almost became a straight line along with a high value of coercivity (Fig. 8d) which supported the previous discussion along with an increase in surface anisotropy at higher temperature. Uncompensated spins at the surface produced a ferromagnetic like behavior, giving rise to remanence and coercivity in the hysteresis loops.²

4. Implication for waste water disposal: photodecomposition of phenol

We studied the semiconductor photocatalyst activity of NiO for the photodegradation of phenol. Phenol is a major pollutant of surface and/or groundwater and according to environment protection rules of World Health Organization (WHO) the exposure limit of phenol in inland water should be lower than 0.02 mg L^{-1} (1994) and its degradation to a safe level in this range is very difficult due to its stability and solubility in water. Though NiO is reported as a catalyst for oxidation of numerous alcohols,⁵³ its photocatalytic activity was rarely explored.^{20,54}

In the present work we investigated the dependence of morphology of NiO NPs with photocatalytic efficiency by monitoring the characteristic fluorescence emission of phenol at 305 nm (Fig. 9). In every case the emission peak at 305 nm diminished gradually as the exposure time increased. For NiO I the emission peak intensity decreased up to 82% which indicated the percentage of phenol degraded. Conversely for commercial NiO nanopowder the level of decrease was $\sim 44\%$. The decrease of the emission peak intensity at 305 nm is attributed to the degradation of phenol under the irradiation of ultraviolet light and hence our synthesized NiO NPs (Fig. 9b, c) showed good photocatalytic reactivity in the decomposition of phenol. Nickel oxides were used as catalyst for another three cycles (Fig. S4, ESI†). For each cycle the percentage of phenol degraded is presented in Fig. 9f.

Degradation of phenol corresponds to hydroxylation of the phenyl ring⁵⁵ as promoted by hydroxyl radicals ($\cdot\text{OH}$). The $\cdot\text{OH}$ radicals are formed by combination of water with electron-hole pairs in nickel oxide formed due to adsorption of phenol on the surface of NiO and irradiation by UV light, while electrons convert oxygen to superoxide radicals ($\cdot\text{O}_2^-$), which are also highly active oxidizing species. In aqueous solution the holes are scavenged by surface hydroxyl groups to generate strongly oxidizing hydroxyl radicals ($\cdot\text{OH}$). Some other reactive species such as $\text{HO}_2\cdot$ and H_2O_2 were also formed during the reaction. The mechanistic pathway is shown in Scheme 2.

When phenol molecules are adsorbed on the surface of excited NiO nanoparticles, they obtain the necessary activation energy to react with $\cdot\text{OH}$ radicals and produce CO_2 and H_2O ⁵⁶ where intermediates *viz.*, catechol, hydroxyhydroquinone, hydroquinone, benzoquinone *etc.* were also expected to form.^{57,58}

The Brunauer–Emmett–Teller (BET) surface area of NiO prepared by method I (granular shaped) was much higher than that prepared by method II (hexagonal shaped) for SDS/CTAB ratio 65/35 elucidated by N_2 sorption analysis (Table 3). The increase in surface area for NiO I may be attributed to its smaller grain size. The number of active surface sites is high in NiO I and consequently the surface charge carrier transfer rate in photocatalysis was higher than for NiO II. Since there are a very few reports on the photocatalytic activity of NiO on water pollutants, our findings suggested a useful environmental application of nanostructured NiO for removal of organic pollutant, air purification, and waste-water remediation.

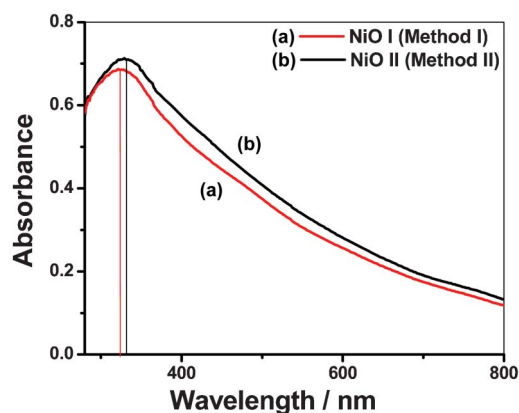


Fig. 7 Absorption spectra of NiO synthesised by method I (a) and method II (b).

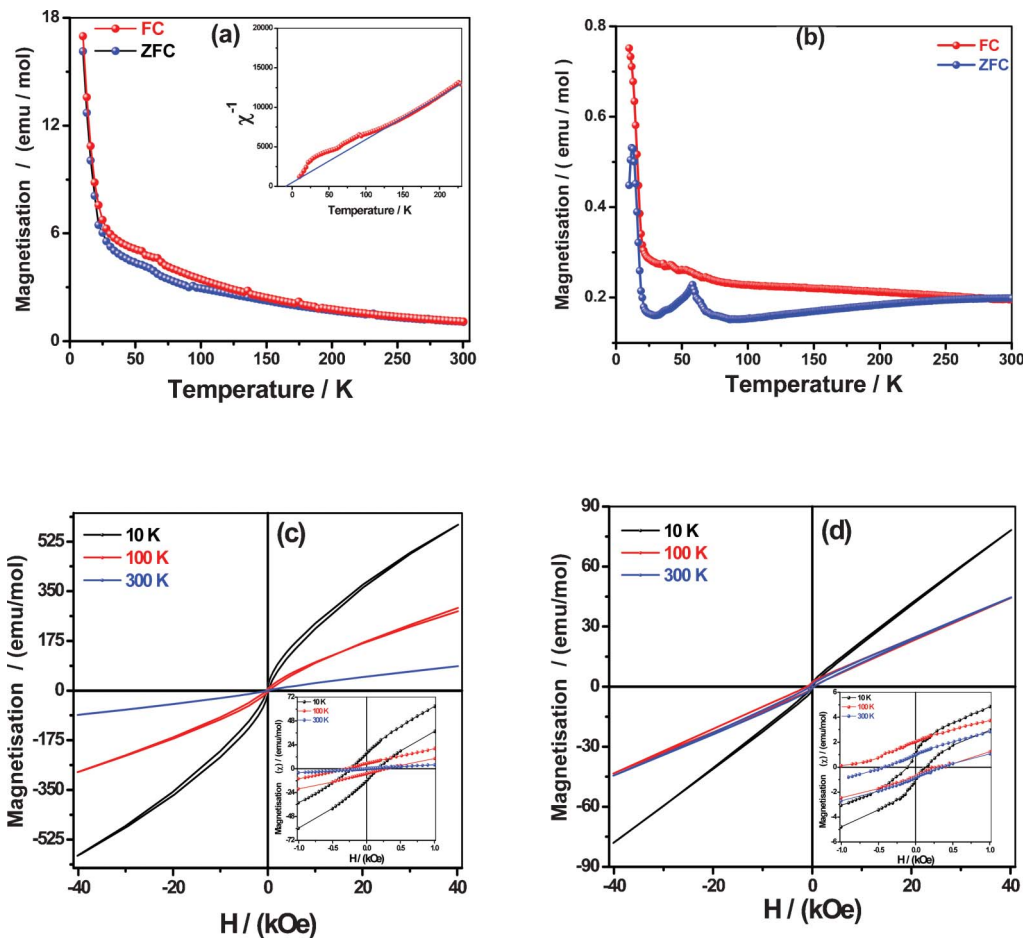


Fig. 8 Magnetization curve of NiO I (a) and NiO II (b) for ZFC and FC in a 50 Oe applied field as a function of temperature (inset shows a plot of χ^{-1} vs. T for NiO I) and (c), (d) their corresponding magnetic hysteresis loops (inset shows magnified hysteresis loops from -1000 to 1000 Oe).

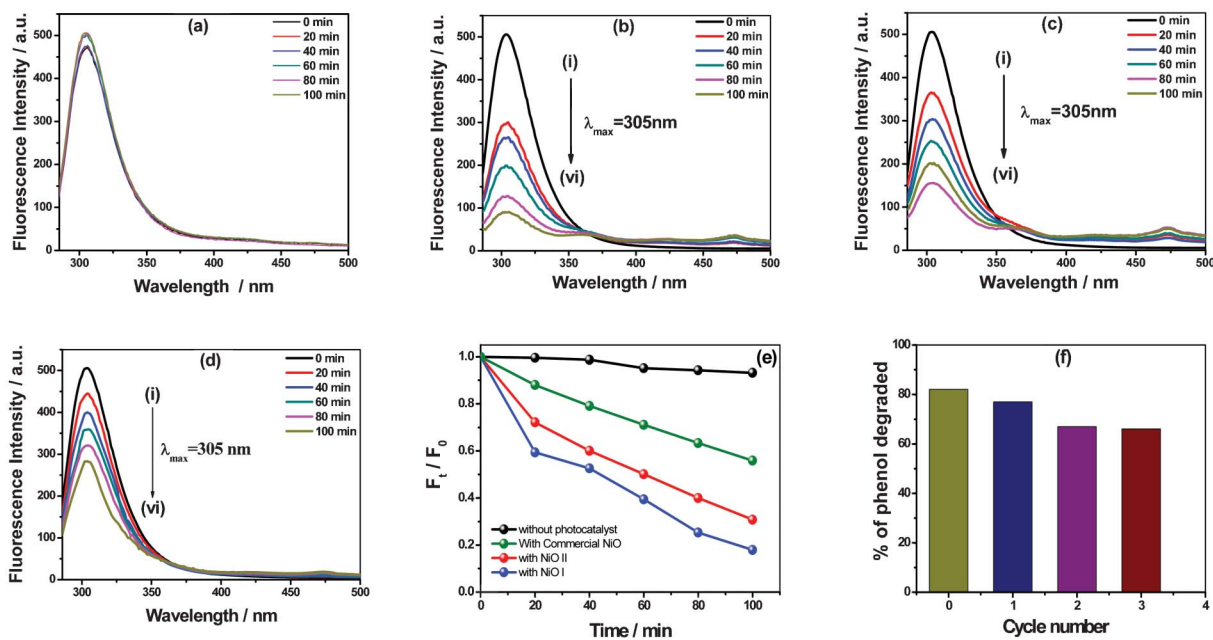
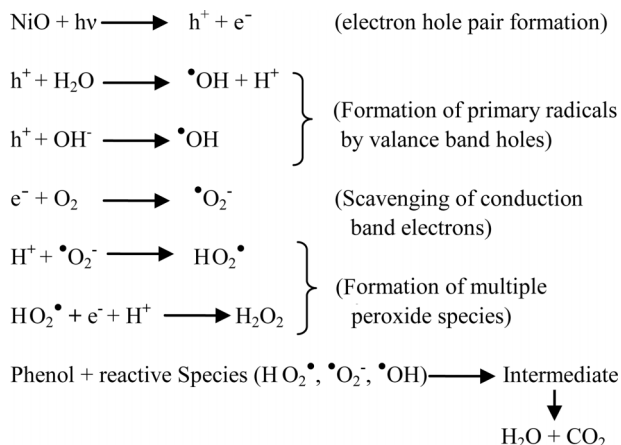


Fig. 9 Photoluminescence spectra of residual phenol under UV light excitation in presence of (a) no catalyst, (b) NiO I, (c) NiO II and (d) commercial NiO nanopowder, (e) intensity of residual phenol as a function of UV irradiation time, (f) value of percentage of phenol degraded for each cycle for NiO I as a catalyst.



Scheme 2 Possible photodegradation pathway of phenol over NiO.

Conclusion

In summary, we designed a soft and facile cationic surfactant controlled approach for preparation of various nickel oxalate nanostructures, including single layered nanosheets, multilayered nanosheets and nanoflakes. Compared with other conventional solution methods, this technique avoids large concentration gradients and gives better control of the particle growth in chemical processing systems. The role of the cationic surfactant in controlling the morphology of nickel oxalate has been studied in detail in the anionic rich region. After calcination in air, the as-prepared nickel oxalate single layered nanosheets are converted to NiO nanostructures with different grain size and morphology. Magnetic study of NiO with size 5–10 nm shows canted antiferromagnetism but for 22–27 nm grain size, we find surface spin disorder resulting in spin glass behaviour. The as-obtained NiO nanostructures show high photocatalytic activity to decompose phenol dissolved in water displaying great potential in the application of environmental pollutant cleanup. This easy but efficient approach presented here, not only can be extended for the synthesis of other metal oxides with controlled shape and structure but also fundamentally provides a new route towards fabrication of inorganic materials into well-defined morphologies for potential applications.

Acknowledgements

S. R and S. S. M acknowledges UGC for providing JRF. S. C, S. B and S. P. M greatly appreciate the funding from DST (SR/S1/PC-63/2009). Authors are grateful to Dr K. K. Chattopadhyay, Mr N. S. Das and Mr D. Sarkar of Jadavpur University, India for their kind help in performing TEM and FESEM measurements. The authors also thank Dr S. Koner, Jadavpur University, India for his help in BET surface area measurement. The authors are also thankful to the reviewers for their valuable suggestions.

References

- V. Protasenko, D. Bacinello and M. Kuno, *J. Phys. Chem. B*, 2006, **110**, 25322.
- R. H. Kodama, S. A. Makhlof and A. E. Berkowitz, *Phys. Rev. Lett.*, 1997, **79**, 1393.
- S. Chall, A. Saha, S. K. Biswas, A. Dutta and S. C. Bhattacharya, *J. Mater. Chem.*, 2012, **22**, 12538.
- N. Tian, Z. Y. Zhou, S. G. Sun, Y. Ding and Z. L. Wang, *Science*, 2007, **316**, 732.
- C. Burda, X. B. Chen, R. Narayanan and M. A. El-Sayed, *Chem. Rev.*, 2005, **105**, 1025–1102.
- J. T. Sampanthar and H. C. Zeng, *J. Am. Chem. Soc.*, 2002, **124**, 6668.
- Y. Hou, H. Kondoh, M. Shimojo, T. Kogure and T. Ohta, *J. Phys. Chem. B*, 2005, **109**, 19094.
- X. Wang, X. Chen, L. Gao, H. Zheng, M. Ji, C. Tang, T. Shen and Z. Zhang, *J. Mater. Chem.*, 2004, **14**, 905.
- F. Cai, G. Zhang, J. Chen, X. Gou, H. Liu and S. Dou, *Angew. Chem., Int. Ed.*, 2004, **43**, 4212.
- J. Park, E. Kang, S. U. Son, H. M. Park, M. K. Lee, J. Kim, K. W. Kim, H. J. Noh, J. H. Park, C. J. Bae, J. G. Park and T. Hyeon, *Adv. Mater.*, 2005, **17**, 429.
- X. Wang, J. Song, L. Gao, J. Jin, H. Zheng and Z. Zhang, *Nanotechnology*, 2005, **16**, 37.
- P. Poizot, S. Laruelle, S. Grugeon, L. Dupont and J. M. Tarascon, *Nature*, 2000, **407**, 496.
- X. Wang, L. Li, Y. G. Zhang, S. T. Wang, Z. D. Zhang, L. F. Fei and Y. T. Qian, *Cryst. Growth Des.*, 2006, **6**, 2163.
- M. C. A. Fantini, F. F. Ferreira and A. Gorenstein, *Solid State Ionics*, 2002, **152–153**, 867.
- T. Ahmad, K. V. Ramanujachary, S. E. Lofland and A. K. Ganguli, *Solid State Sci.*, 2006, **8**, 425.
- H. Pang, Q. Lu, Y. Lia and F. Gao, *Chem. Commun.*, 2009, 7542.
- S. D. Tiwari and K. P. Rajeev, *Thin Solid Films*, 2006, **505**, 113.
- X. Song, L. Gao and S. Mathur, *J. Phys. Chem. C*, 2011, **115**, 21730.
- S. Mohan, P. Srivastav, S. N. Maheshwari, S. Sundarb and R. Prakash, *Analyst*, 2011, **136**, 2845.
- X. Wang and L. Gao, *J. Phys. Chem. C*, 2008, **112**, 15299.
- D. Wang, C. Song, Z. Hu and X. Fu, *J. Phys. Chem. B*, 2005, **109**, 1125.
- L. Dong, Y. Chu and W. Sun, *Chem.–Eur. J.*, 2008, **14**, 5064.
- S. Vaidya, P. Rastogi, S. Agarwal, S. K. Gupta, T. Ahmad, A. M. Antonelli Jr., K. V. Ramanujachary, S. E. Lofland and A. K. Ganguli, *J. Phys. Chem. C*, 2008, **112**, 12610.
- M. S. Bakshi, G. Kaur, P. Thakur, T. S. Banipal, F. Possmayar and N. O. Petersen, *J. Phys. Chem. C*, 2007, **111**, 5932.
- K. Holmberg, *J. Colloid Interface Sci.*, 2004, **274**, 355.
- A. Caria and A. Khan, *Langmuir*, 1996, **12**, 6282.
- H. Edlund, A. Sadaghiani and A. Khan, *Langmuir*, 1997, **13**, 4953.
- E. F. Marques, O. Regev, A. Khan, M. G. Miguel and B. Lindman, *J. Phys. Chem. B*, 1998, **102**, 6746.
- H. Shi, L. Qi, J. Ma, H. Cheng and B. Zhu, *Adv. Mater.*, 2003, **15**, 1647.
- Y. Xing, M. Li, S. A. Davis, A. J. Patil and S. Mann, *Soft Matter*, 2006, **2**, 603.

- 31 H. Shi, X. Wang, N. Zhao, L. Qi and J. Ma, *J. Phys. Chem. B*, 2006, **110**, 748.
- 32 S. Ahmed, M.G. Rasul, W. N. Martens, R. Brown and M.A. Hashib, *Desalination*, 2010, **261**, 3.
- 33 S. L. Koro and L. Dekany, *Colloids Surf., A*, 2006, **280**, 146.
- 34 J. Sato, H. Kobayashi and Y. Inoue, *J. Phys. Chem. B*, 2004, **108**, 4369.
- 35 L. V. Dearden and E. M. Woolley, *J. Phys. Chem.*, 1987, **91**, 2404.
- 36 B. S. Furniss, A. J. Hannaford, P. W. G. Smith and A. R. Tatchell, *Vogel's Textbook of Practical Organic Chemistry*, Longman Singapore Publishers Pte. Ltd, Singapore, 5th edn., p. 408.
- 37 P. Mukerjee and K. J. Mysels, *NSRDS-NBS 36*, US Government Printing Office, Washington, D. C., 1971.
- 38 K. Kalyanasundaram and J. K. Thomas, *J. Am. Chem. Soc.*, 1977, **99**, 2039.
- 39 S. Thota and J. Kumar, *J. Phys. Chem. Solids*, 2007, **68**, 1951.
- 40 B. Tah, P. Pal, M. Mahato and G. B. Talapatra, *J. Phys. Chem. B*, 2011, **115**, 8493.
- 41 P. Andreozzi, S. S. Funari, C. La Mesa, P. Mariani, M. G. Ortore, R. Sinibaldi and F. Spinozzi, *J. Phys. Chem. B*, 2010, **114**, 8056.
- 42 V. Tomašić, I. Štefanić and N. Filipović-Vinceković, *Colloid Polym. Sci.*, 1999, **277**, 153.
- 43 C. Leitiza, P. Andreozzi, A. Scipioni, C. La Mesa, A. Bonincontro and E. Spigone, *J. Phys. Chem. B*, 2007, **111**, 898.
- 44 S. S. Kim, Y. Liu and T. J. Pinnavaia, *Microporous Mesoporous Mater.*, 2001, **44–45**, 489.
- 45 D. Wang, Q. Wang and T. Wang, *Inorg. Chem.*, 2011, **50**, 6482.
- 46 K. Karthik, G. K. Selvan, M. Kanagaraj, S. Arumugam and N. V. Jaya, *J. Alloys Compd.*, 2011, **509**, 181.
- 47 V. Bisht, K. P. Rajeev and S. Banerjee, *Solid State Commun.*, 2010, **150**, 884.
- 48 S. A. Makhlof, F. T. Parker, F. E. Spada and A. E. Berkowitz, *J. Appl. Phys.*, 1997, **81**, 5561.
- 49 R. K. Mishra, D. K. Pradhan, R. N. P. Choudhary and A. Banerjee, *J. Magn. Magn. Mater.*, 2008, **320**, 2602.
- 50 S. Xiang, X. Wu, J. Zhang, J. Zhang, R. Fu, S. Hu and X. Z. Zhang, *J. Am. Chem. Soc.*, 2005, **127**, 16352.
- 51 M. Y. Ge, L. Y. Han, U. Wiedwald, X. B. Xu, C. Wang, K. Kuepper, P. Ziemann and J. Z. Jiang, *Nanotechnology*, 2010, **21**, 425702.
- 52 H. Bi, S. Li, Y. Zhang and Y. Du, *J. Magn. Magn. Mater.*, 2004, **277**, 363.
- 53 S. Thota and J. Kumar, *J. Phys. Chem. Solids*, 2007, **68**, 1951.
- 54 S. T. Christoskova and M. Stoyanova, *Water Res.*, 2002, **36**, 2297.
- 55 T. Zhu, J. S. Chen and X. W. (David) Lou, *J. Phys. Chem. C*, 2012, **116**, 6873.
- 56 D. Li and H. Haneda, *Chemosphere*, 2003, **51**, 129.
- 57 A. Sobczynski, L. Duczmal and W. Zmudzinski, *J. Mol. Catal. A: Chem.*, 2004, **213**, 225.
- 58 K. I. Okamoto, Y. Yamamoto, H. Tanaka and M. Tanaka, *Bull. Chem. Soc. Jpn.*, 1985, **58**, 2015.